Chapter 04: Copper-Mould Casting of Alloys

4.1 Introduction

Metallic glasses (MGs) displaying large section thickness and high glass-forming abilities are known as Bulk Metallic Glasses (BMGs)[4]. These materials have a combination of properties such as high mechanical strength[157], high hardness[120], [122], good thermal stability, and large supercooled liquid region[157], [158]. BMGs have given fresh impetus to the researchers on MG. Fe-based amorphous are always different from other BMGs because it has a combination of metal-metalloids [22], [29], [159], [160]. Owing to the presence of metalloids in these alloys, the local clusters present in the liquid alloy are likely to be different from other MGs[22] without metalloids. It is believed that the local structure in liquid alloys frozen in the amorphous state may slightly change and facilitate the nucleation of nano-crystals depending on the processing conditions. The current version of Fe-based BMGs has attracted attention for their envisaged applications as structural materials [4], [32]. They are non-magnetic also. Owing to their limitation of ductility of structural amorphous steels (SASs), the researchers have been trying to optimize the microstructures through the design of nano BMG composites, so that the optimum combination of properties is achieved [161], [162]. Fe-Mn-Cr-Mo-C-B-Y compositions as BMGs have been shown to possess a density of 7.8g/cc (maraging steels have a density ~8.1 g/cc) and hardness value more than that of maraging steels [40][163]. Owing to this, it is important to study the variation of compositions in Fe-Mn-Cr-Mo-C-B-Y substituting some of the known elements facilitates glass forming abilities, it is appropriate to look for alternate processing routes to study the behavior of these alloys under different processing conditions as will be discussed in chapter 05, and 06. The selection of alloying elements in such a way they shift the C-curve (cooling curve) for the liquid-solid transformation to the right that suggests that the liquid can be retained in the super-cooled condition for a longer period, therefore the value of critical cooling rate (R_c) for glass formation is lower. This is the concept that is utilized in the synthesis of BMGs which contain a large number of alloying elements[164]. Various casting techniques are used by researchers for the formation of BMGs. The first Fe-based BMG in a Fe-Al-Ga-P-C-B system in 1995 was synthesized by Inoue and his Co-worker[165]. Gu et al.[148], successfully synthesized $Fe_{61}Cr_4Mo_{14}C_{15}B_6$ BMG of 2 mm rod in Suction-casting into Cu-mould casting technique. The Young's modulus and Poisson ratio of the BMGs are 204 GPa and 0.32 respectively. Iqbal et al.[121], synthesized Fe48Cr15Mo14C15B6Y2 BMG of 4 mm diameter rod by using injection

into Cu-mould. Liang et al.[122], successfully produced a 6 mm diameter BMG of composition $Fe_{45}Cr_{20}Mo_{10}W_2C_{15}B_6Y_2$ by using drop cast into Cu-mould technique. Lu et al.[40], studied three different Fe-based BMG compositions for structural applications. They compared the hardness to density (H/ρ) ratio of these BMGs with the maraging steels and concluded that it is four times more than maraging steel.

4.2 Experimental Procedure

Four alloys, whose nominal compositions are given in Table 3.1 in the previous chapter 03 were prepared by conventional Cu-mould casting technique. The master alloy utilized for making them was grey cast iron whose composition is also given in Table 3.1. The required amounts of elements in bulk form were added to this cast iron to get nominal compositions. The alloys are designated as A, B, C, and D. The complete information regarding elements added to make alloys was discussed in Chapter 3. A 25g charge of each alloy composition was melted in a Vacuum arc-melting furnace (M/S Vacuum Technologies, Bangalore). Once the metals were melted, the Cu-hearth acted like a heat sink, and heat was extracted from molten alloys to

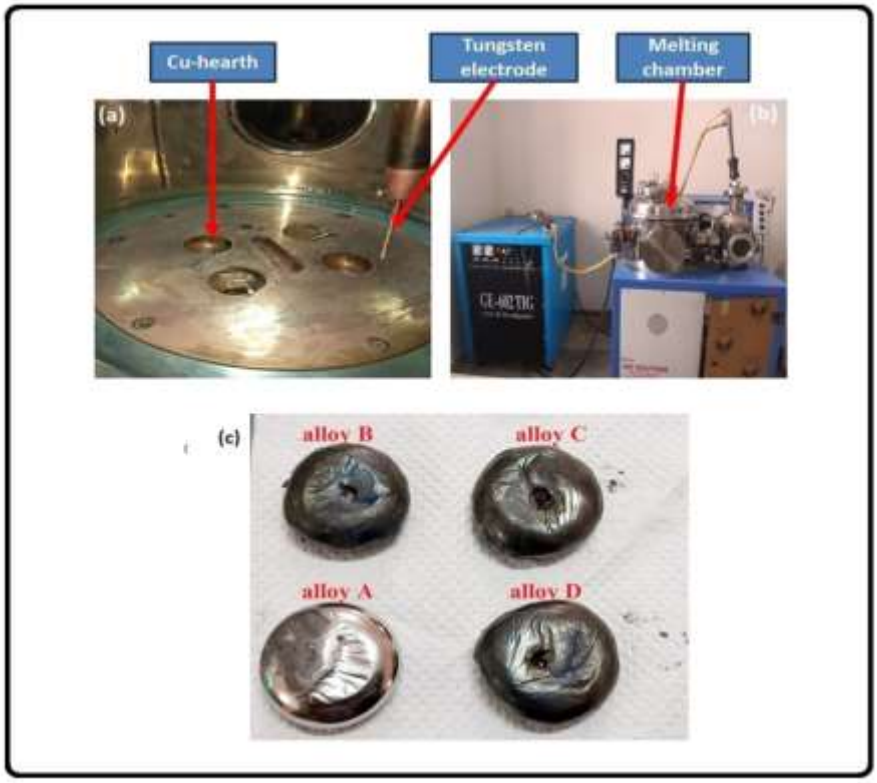

Fig. 4. 1: Optical image of (a) inside view of melting chamber, (b) Vacuum arc melting set-up, and (c) alloys buttons

get solidify. These alloys have shapes like buttons of 30 mm diameter and 10mm thickness. To avoid oxidation Ti-getters were used in the presence of argon atmosphere. In order to obtain homogeneity, the molten alloys were stirred and re-melted at least four times. An optical image of the arc melting furnace unit and alloy buttons produced by it are shown in Fig.4.1(a)-(c). The Archimedes principle was used to measure the bulk densities of these alloys prepared by Cu-mould casting. The investigation of structure and phases evolve in as-cast alloys was carried out X-ray diffraction (MiniFlex600, RIGAKU) instrument using a Cu-K_α (λ=1.541A^o) radiation source. The operating voltage and current were kept at 40kV and 15mA respectively. All the samples are cut in the required shape and put on the sample holder. All the samples were scanned from 2θ=20 to 100^o angle with a step size of 0.02^o. The interpretation of X-ray diffraction patterns was finalized with the help of standard JCPDS/ICDD data cards. The required size of alloys was taken for metallographic examination by following standard procedures for specimen preparation. The freshly prepared etchant with 5% nitric acid and 95% ethanol solution (Nital) was used for revealing their microstructures under an optical microscope (OM) (Leica model LV 500). The thermal stability of the alloys was investigated by differential scanning calorimetry (DSC) at a heating rate of 20 ^{O}C/min under a continuous flow of nitrogen gas. The indentation characteristics are measured by an instrumented micro-hardness tester (Anton Parr: MHT^3). A Vickers diamond indenter was used. Indentation load applied from 10mN to up to fracture of the specimen with 20 sec of dwell time. At least ten indentations were reported here for reproducing the results.

4.3 Results

4.3.1 Density Measurement

The Archimedes principle was used for the measurement of density(ρ) of as-cast samples. The measured values of the density of these alloys are given in Table 4.1.

Table 4. 1: The bulk (experimental) density of Cu-mould cast alloy

Sl.no.	Alloy Compositions (at. %)	Bulk Density(g/cc)
A	Fe56.24Cr4Mo14C15Si3.8B6	7.47
B	Fe43.47Cr15Mo14C15.12Si3.78B6Y2	7.65
C	Fe40.2Cr20Mo10W2C15Si4.2B6Y2	7.47
D	Fe40.2Cr15Mo14Co3C15Si4.2B6Y2	7.30

4.3.2 Evolution of Microstructures

Figure 4.2, shows the optical micrograph of the master alloy i.e. cast iron (C.I.), whose composition is mentioned in Table 3.1. The microstructure shown in Fig.4.2 (a) without the etch condition has long flakes of graphite embedded in an iron matrix of master alloy. Generally, flaky graphite is observed in grey cast iron. It is confirmed that this micrograph is very similar to grey cast iron. A picral reagent (4% in vol. %) was used to reveal the microstructure of cementite (Fe_3C). Cementite nodules with very fine flakes of graphite are produced after using etchant, as shown in Fig. 4.2 (b). The graphite flakes occupied a large area as compared to cementite.

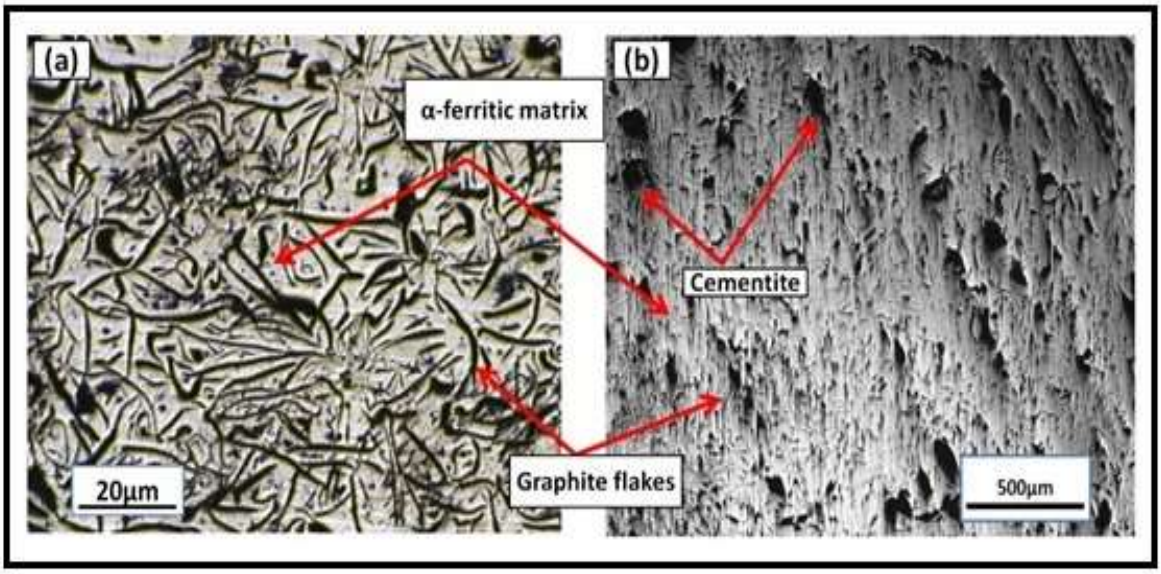

Fig. 4. 2: Optical micrograph of master alloy (cast-iron), (a) without etched condition and (b) etched with 4% picral (vol. %) solution

The evolutions of microstructures due to the addition of alloying elements in Cu-mould cast alloys were investigated. For this, the first samples were cold mounted by using Bakelite powder, and then grinding, cloth polishing, and then polished with 200,600, 1000, and 1200 grit silicon carbide paper. Finally, very fine polishing was done with 0.5µm diamond paste to obtain a mirror-like polish surface. After that samples were etched with 5% nital solution (vol. %), the microstructure has been shown in Fig. 4.3 (b). Different areas were chosen from sample space at different magnifications for observation of uniformity in microstructures. The micrographs of alloy-A depict dendrites are formed in some regions. The natures of dendrites are primary dendrites type only. This type of microstructure is very similar to class 30 grey cast-iron[166] as shown in fig4.3 (a). In which ferrite dendrites and graphite are developed in a ferrite matrix. Similarly in the

present microstructure perlite is formed in a cementite matrix. The microstructure developed in alloy-A is not uniform. It may be due to variations in the cooling rate inside the Cu-mould.

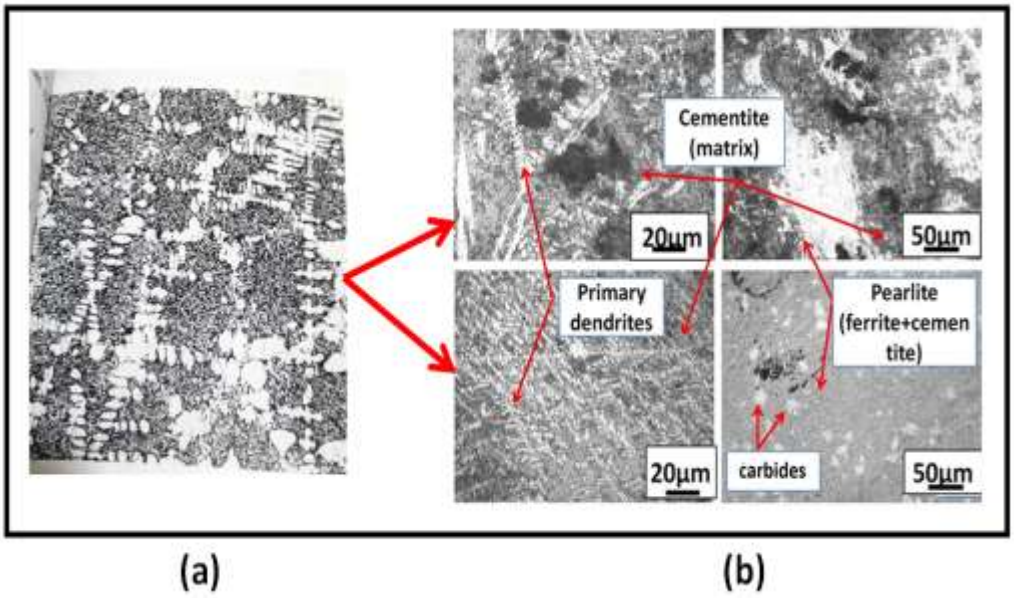

Fig. 4. 3: (b) Optical micrograph from different regions of Cu-mould cast alloy-A, etched with 5% nital, (a) Class 30 grey cast iron, ferrite dendrites and graphite in a ferrite matrix (ASM Metal Handbook, Vol. 9)[166].

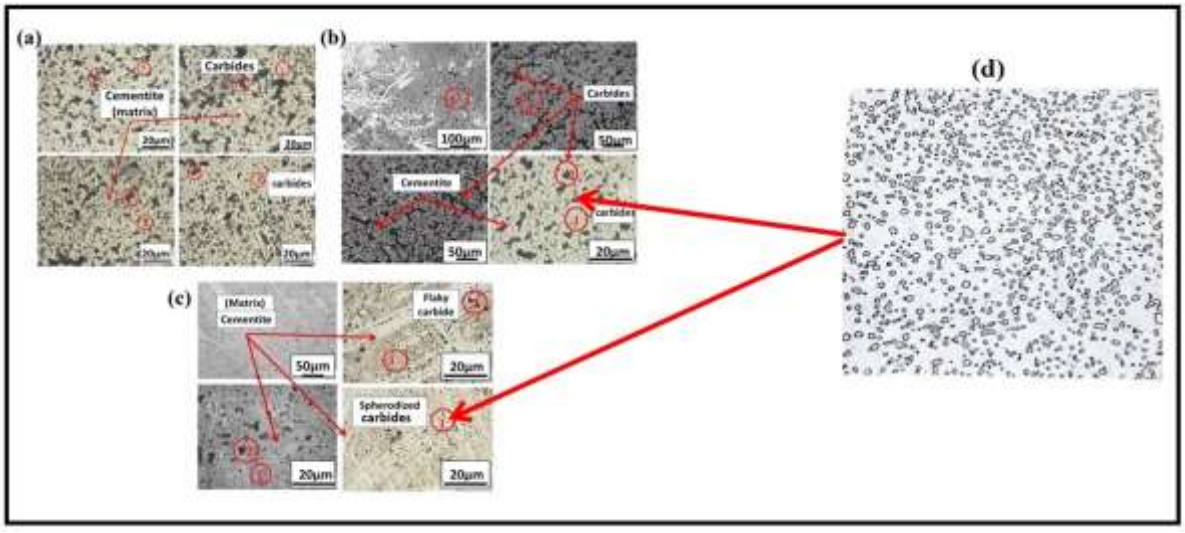

Fig. 4. 4: (a-c) Optical micrograph of alloys-A, B, and C respectively, shows cementite matrix embedded with flaky (irregular dark color) cementite and spheroidized (light grey color dots) carbides: (d) microstructure of AISI 1074 steel, spheroidized carbides in ferrite matrix (ASM handbook, vol.9, page no.261)[166].

The evolution of microstructures in alloy-B, alloy-C, and alloy-D after the addition of Yttrium (Y), is shown in Fig. 4.4 (a-c) respectively. The micrograph of these alloys depicts a cementite matrix embedded with flaky (irregular dark color) cementite and spheroidized (light grey color dots) carbides. This is similar to that observed in AISI 1074 steel[166] as shown in Fig. 4.4 (d). In their microstructure, the spheroidized carbides are formed in a ferritic matrix. Alloy-B, alloy-C, and alloy-D have formed similar kinds of microstructures. However, the volume fraction of carbide formation is different.

4.3.3 Structural and Phase Characterization: X-ray diffraction

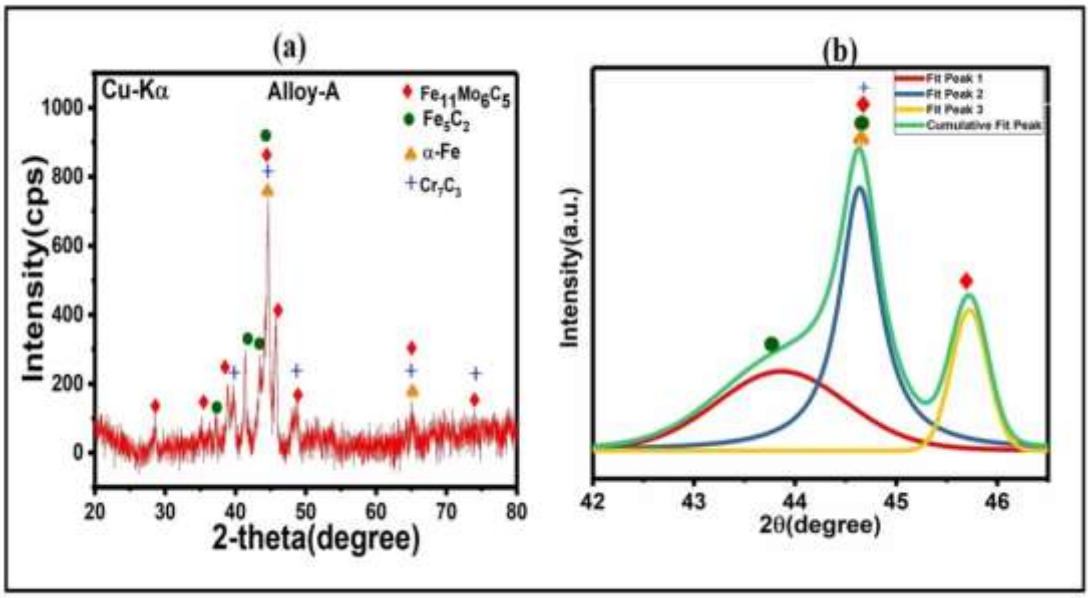

Fig. 4. 5: (a) X-ray diffraction pattern of as-cast alloy-A ($Fe_{56.24}Cr_4Mo_{14}C_{15}Si_{3.8}B_6$); (b) deconvolution of intense peaks

I have marked the phases with appropriate legends as shown in the X-ray diffraction results for the entire alloy-A, B, C, and D in Fig. (4.5-4.8). The details of the expected phases along with the respective d-spacing and corresponding hkl planes are given in Table-4.2 to 4.5 respectively.

Table 4. 2: The d-spacing values corresponding to their (hkl) planes of the observed phases in Alloy-A

Experimentally observed d-spacing	**d-spacing in A^o (hkl) of expected phases**			
d(in A^o)	**$Fe_{11}Mo_6C_5$**	**α-Fe**	**Cr_7C_3**	**Fe_5C_2**
3.125	3.085(221)	-	-	-
2.550	2.541(402)	-	-	-
2.419	-	-	-	2.421(311)
2.318	2.340(400)	-	-	-
2.271	-	-	2.263(200)	-
2.186	-	-	-	2.208(112)
2.084	-	-	-	2.083(021)
2.032	2.055(511)	2.026 (100)	2.046(124)	2.053(510)
1.979	2.011(420)	-	-	-
1.869	1.864(401)	-	1.878(221)	-
1.431	1.431(332)	1.433(200)	1.433(234)	-
1.376	-	-	1.376(241)	-
1.264	1.263(061)	-	1.261(244)	-

The X-ray diffraction patterns of Cu-mould cast product (i.e., alloy-A) having nominal composition $Fe_{56.24}Cr_4Mo_{14}C_{15}Si_{3.8}B_6$ are shown in fig.4.5 (a). It was shown that multiple crystalline peaks with several phases are evolved in alloy-A. Most of the peaks have intermetallic phases. The phases evolved have structure types of α-Fe (cI2), $Fe_{11}Mo_6C_5$ (mC44), Fe_5C_2 (mC28), and Cr_7C_3 (oP44). The shouldering and splitting of peak cross-ponding to maximum intense and moderate intense peaks indicate that there are mixtures of phases are present in the sample. The peak splitting at the intense peak was deconvoluted and had a spread of 2θ 42^o to 46^o as shown in Fig.4.5 (b) in as-cast alloys A. The deconvolution result shows that this peak consists of three peaks of different phases. The 2θ positions of evolved phases after the deconvolution of these peaks are given in Table 4.6. In the XRD pattern alloy-B as shown in Fig. 4.6 some new crystalline and more intense peaks were observed after the addition of Y (2 at%). Alloy-B has been found in some common phases (α-Fe, $Fe_{11}Mo_6C_5$, and Cr_7C_3) as found in alloy-A. A new phase was

evolved having a structure of Fe_3W_3C (cF112) type. The maximum intense peak was observed at a Bragg angle of 2θ= ~ 42° that has a d-spacing of 2.14 A°. The d-spacing of this intense peak is matched with three phases $Fe_{11}Mo_6C_5$, Cr_7C_3, and Fe_3W_3C.

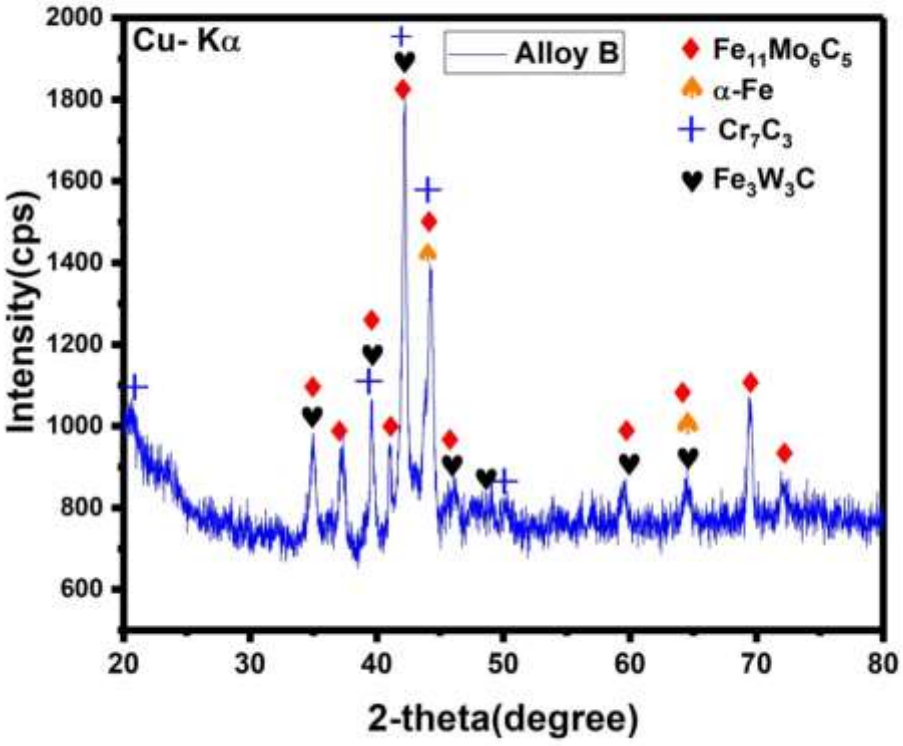

Fig. 4. 6: X-ray diffraction pattern of as-cast alloy-B ($Fe_{43.47}Cr_{15}Mo_{14}C_{15.12}Si_{3.78}B_6Y_2$)

Similarly in alloy-C after the addition of W (2at %), a new phase cementite Fe_3C having oP116 type structure is formed as shown in the XRD pattern in Fig. 4.7(a). It was observed that the position of the maximum intense peak was displaced from the previous one and it formed at 2θ = ~45° with d-spacing of 2.01A°. This d-spacing matches with three phases, $Fe_{11}Mo_6C_5$, Fe_3C, and α-Fe. It was also observed that the shouldering or splitting of intense peaks has been seen

Table 4. 3: The d-spacing values corresponding to their (hkl) planes of the observed phases in Alloy-B

Experimentally observed d- spacing	**d-spacing in Aº (hkl) of expected phases**			
d(in Aº)	**$Fe_{11}Mo_6C_5$**	**α-Fe**	**Cr_7C_3**	**Fe_3W_3C**
2.566	2.540(402)	-	-	2.548(331)
2.415	-	-	-	-
2.277	2.290(022)	-	2.294(031)	2.267(422)
2.201	2.202(311)	-	-	-
2.141	2.104(331)	-	2.120(202)	2.138(511)
2.045	2.063(403)	2.026(100)	2.046(131)	-
1.964	-	-	-	1.964(440)
1.819	1.813(241)	-	1.814(204)	-
1.552	1.553(623)	-	-	1.555(551)
1.444	1.447(243)	1.433(200)	-	1.446(553)
1.353	1.354(043)	-	-	1.357(733)
1.311	1.31(134)	-	1.310(323)	-

Therefore, I have to deconvolute the peak in the spread of 2θ =42º to 46º, as shown in Fig 4.7(b). The deconvolution result showed that this peak consists of two peaks at 2θ=44º and 45º. The phases corresponding to it have been given in Table 4.6. Fig. 4.8(a) shows the XRD pattern of alloy-D which represents the crystalline behavior of material. With the addition of Co (3 at %), it has been seen that no change occurred in the intense peak position from the previous one (i.e., in alloy-C). Three crystalline phases (common in all) are formed in alloy-D. They have referred to $Fe_{11}Mo_6C_5$, Cr_7C_3, and α-Fe structure type. The splitting of the peak was also observed at a moderately intense peak. It was deconvoluted with a 2θ spread of 41º to 43º. This result shows that this peak consists of two different phases as given in Table 4.6.

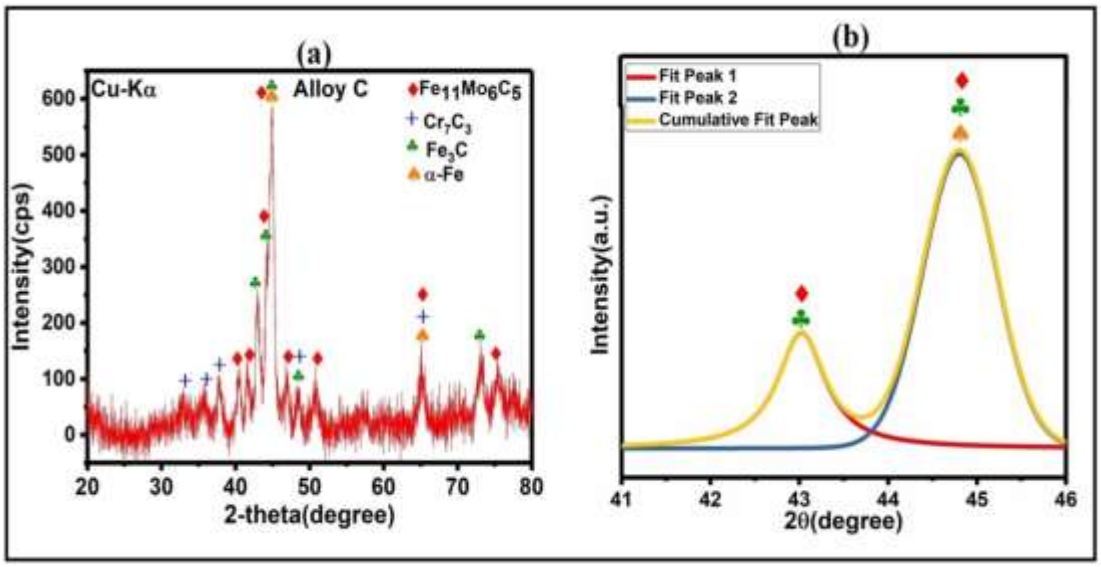

Fig. 4. 7: (a) X-ray diffraction pattern of as-cast alloy-B ($Fe_{40.2}Cr_{20}Mo_{10}W_2C_{15}Si_{4.2}B_6Y_2$) (b) deconvolution of intense peaks with a spread of 2θ of 41°-46°

Table 4. 4: The d-spacing values corresponding to their (hkl) planes of the observed phases in Alloy-C

Experimentally observed d- spacing	**d-spacing in A° (hkl) of expected phases**			
d(in A°)	**$Fe_{11}Mo_6C_5$**	**α-Fe**	**Cr_7C_3**	**Fe_3C**
2.5207	-	-	2.521(122)	-
2.375	-	-	2.372(114)	-
2.235	2.218(421)	-	-	-
2.176	2.172(203)	-	-	-
2.11	2.104(331)	-	-	2.107(211)
2.051	2.055(511)	-	2.046(124)	2.068(102)
2.016	2.011(420)	2.0268(100)	-	2.013(031)
1.937	-	-	-	-
1.885	-	-	1.878(221)	1.879(022)
1.805	1.807(602)	-	-	-
1.608	-	-	1.610(231)	-
1.433	1.431(332)	1.433(200)	1.433(312)	-
1.292	-	-	1.292(109)	1.292(051)
1.258	1.255(205)	-	-	1.252(033)

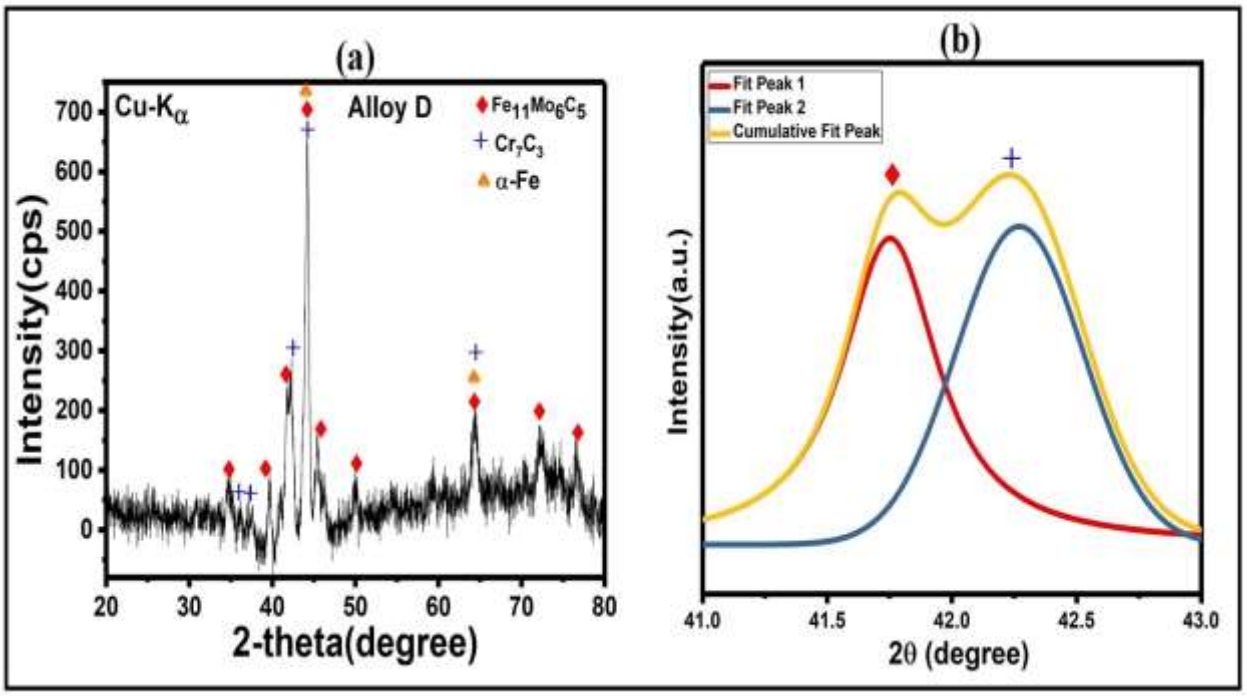

Fig. 4. 8: (a) X-ray diffraction pattern of as-cast alloy-B ($Fe_{40.2}Cr_{15}Mo_{14}Co_3C_{15}Si4.2B_6Y_2$) (b) deconvolution of intense peaks with a spread of 2θ of 41°-43°

Table 4. 5: The d-spacing values corresponding to their (hkl) planes of the observed phases in Alloy-D

Experimentally observed d- spacing	**d-spacing in A° (hkl) of expected phases**		
d(in A°)	**$Fe_{11}Mo_6C_5$**	**α-Fe**	**Cr_7C_3**
2.596	2.540(402)	-	-
2.393	-	-	2.372(114)
2.274	-	-	2.263(200)
2.202	2.202(311)	-	-
2.168	2.170(203)	-	-
2.141	-	-	2.120(202)
2.048	2.055(511)	2.026(100)	2.046(124)
1.996	1.995(113)	-	-
1.819	1.813(241)	-	-

1.556	1.552(623)	-	-
1.449	1.449(151)	1.433(200)	1.449(136)
1.306	1.304(152)	-	-
1.244	1.242(153)	-	-
1.239	1.233(244)	-	-

Table 4. 6: Phases recognised after deconvolution of peaks

Alloy	**2θ(degree)**	**d-spacing (A^o)**	**Phase**	Miller indices (hkl)
Alloy-A	43.8	2.08	Fe_5C_2	(021)
	44.6	2.03	α-Fe	(110)
	45.7	1.98	$Fe_{11}Mo_6C_5$	(113)
Alloy-C	42.8	2.11	$Fe_{11}Mo_6C_5$, Fe_3C	(331), (211)
	44.9	2.01	α-Fe, Fe_3C, $Fe_{11}Mo_6C_5$	(110), (031),(420)
Alloy-D	41.6	2.16	$Fe_{11}Mo_6C_5$	(203)
	42.1	2.14	Cr_7C_3	(105)

4.3.4 Thermal Analysis of as-cast alloys

The thermal stability of as-cast alloys was investigated and the DTA curves of these alloys are shown in Fig. 4.9 (a-d). Alloys were heated up to 1200^{o}C and showed no strong exothermic reactions. It was observed that a small exothermic peak at temperature T1 was found at 870^{o}C in Fig. 4.9(a) and 900^{o}C for alloy A and alloy C respectively. The DTA thermogram tells that the melting points(T2) of alloys A, B, C, and D are found to be 1035^{o}C, 1135^{o}C, 1130^{o}C, and 1145^{o}C respectively. The addition of alloying elements in Fe-Cr-Mo-C-B-Si-based systems has improved the melting point of the as-cast alloys.

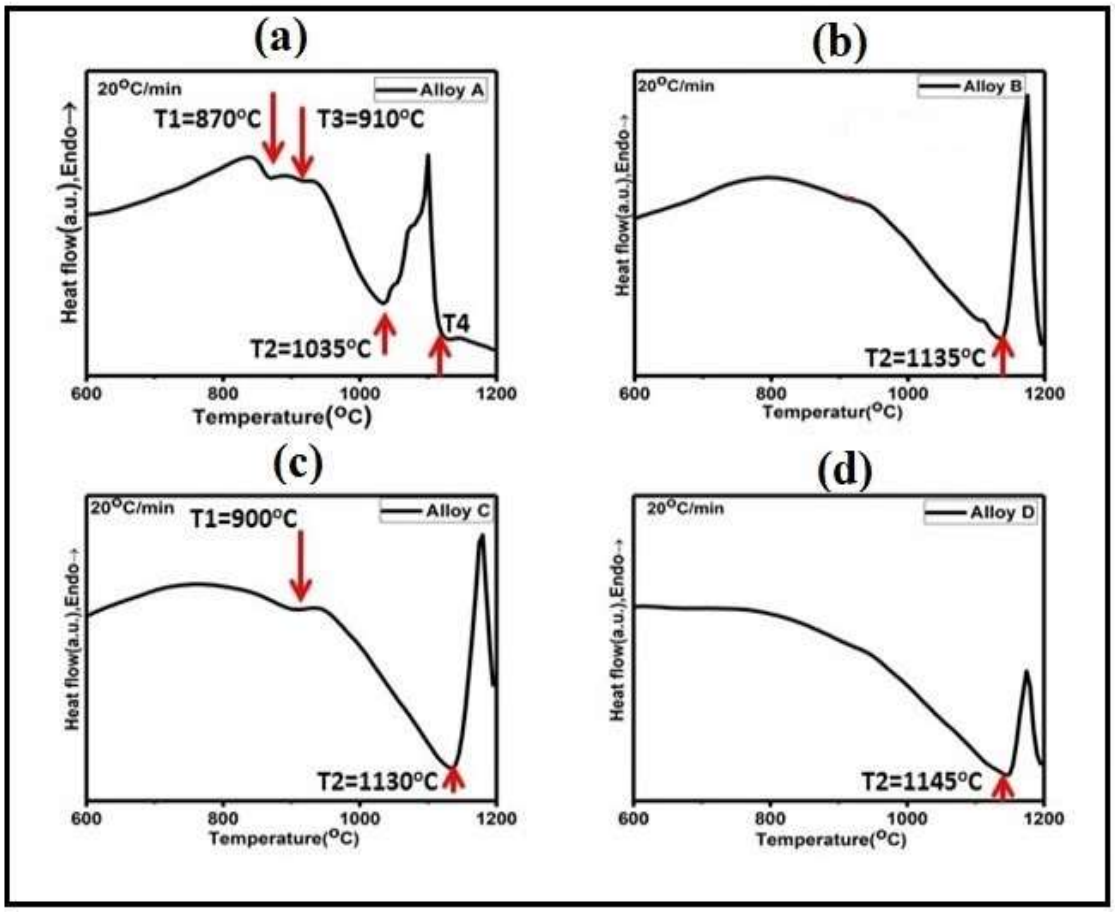

Fig. 4. 9: DTA thermogram of Cu-mould cast alloys, (a) alloy-A, (b) alloy-B, (c) alloy-C, and (d) alloy-D, at a constant heating rate of 20°C/min

4.3.5 Nature of Indentation of as-cast alloy at different loads

The Vickers micro-indentation experiment was carried out to analyze indentation behavior for the Cu-mould cast alloys. Also, this experiment was done for master alloy (i.e., cast iron). The microhardness measurements were carried out at different loads (25g to up to fracture). I have reported here, the mean hardness values of at least ten indentation points on each sample. The distance between neighboring indentations was kept more than three times the diagonal length of each indentation. The indentation impressions of master alloy as shown in fig.4.10, shows that the indentation size increases with load and it is crack free up to 1000g applied load.

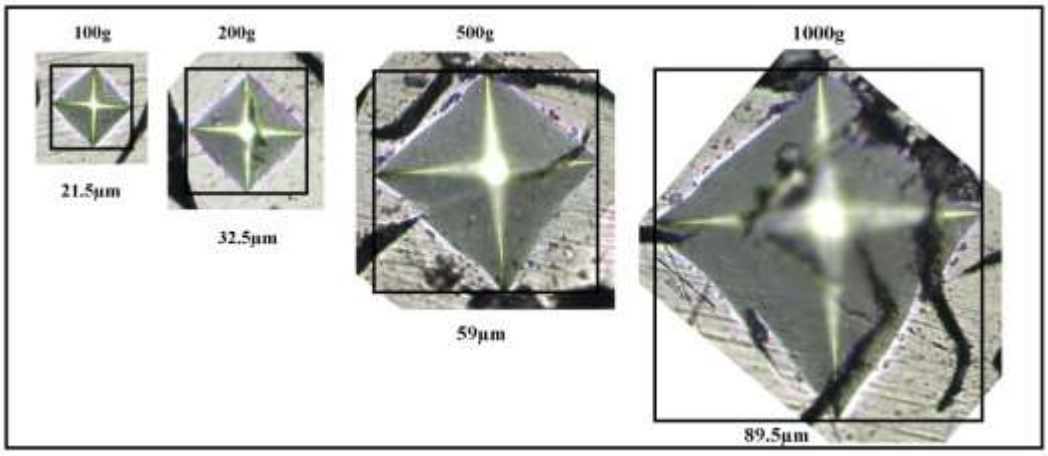

Fig. 4. 10: Optical images of Vickers micro-indentation impressions of master alloy (cast iron) at various loads, showing crack-free up to 1000g indentation load

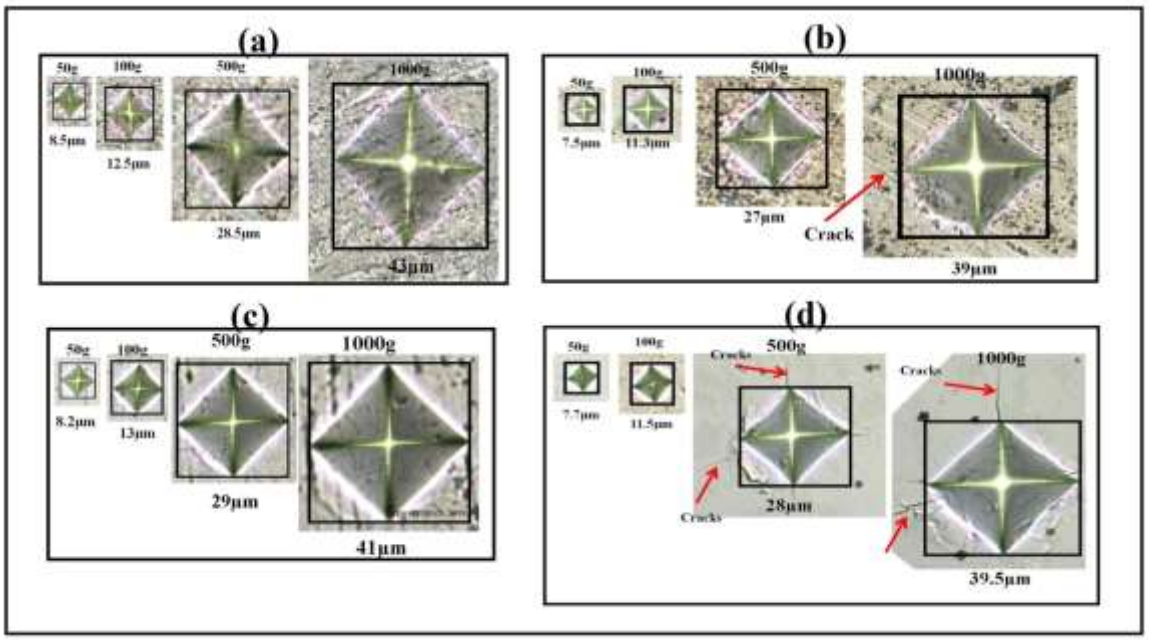

Fig. 4. 11: Optical images of indentation impression from various regions for Cu-mould cast alloys (a) alloy-A, (b) alloy-B, (c) alloy-C, and (d) alloy-D, showing the nature of indentation with load up to fracture

The optical micrograph of alloy-A and alloy-C, as shown in Fig. 4.11(a) and (c) reveals that the indentation impressions are regular and crack-free up to the load 1000g, while it was observed in the case of alloy-B it holds up to 500g and fine crack appeared at their corner at the load applied

to 1000g as shown in fig. 4.11(b). In the case of alloy-D, fine cracks appeared at the corner of the indentation impression at the load of 500g, as shown by the arrow marked in Fig. 4.11(d). The absence of cracks at the corners of Alloy-A and alloy-C suggests that these have better toughness as compared to alloy-B and alloy-D. Alloy-D has very poor toughness among all because it failed earlier. It was observed that the size of the indentation impression increases at a slower rate at low load but it drastically increases at high load conditions. This type of indentation characteristic has been seen in almost all the alloys as shown in Fig. 4.12.

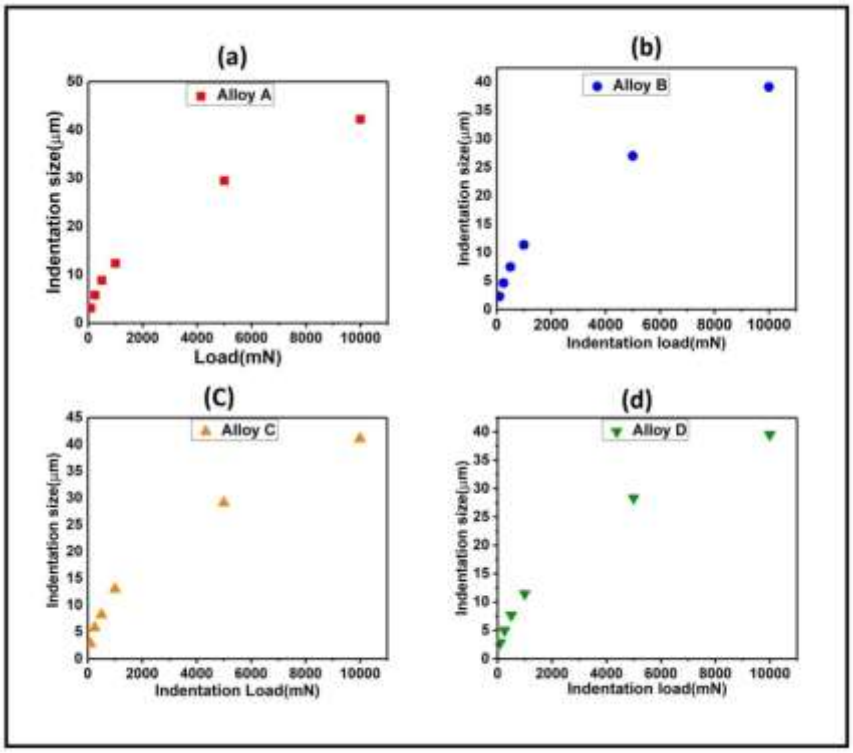

Fig. 4. 12: Shows nature of variation of indentation size with load in (a) alloy A, (b) alloy B, (c) alloy C, and (d) alloy D

The microhardness and elastic modulus were determined from micro indentation experiments for as-cast alloys. The microhardness value of the master alloy is almost constant as the load increases and then decreases as shown in Fig. 4.13. Although the reduced elastic modulus of the master alloy material continuously decreases with increasing load.

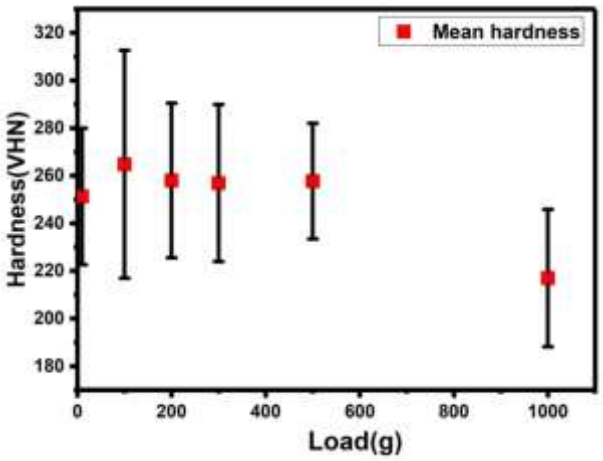

Fig. 4. 13: Variation of hardness (VHN) for load (g) for master alloy (grey cast iron)

Fig. 4.14(a-d) represents the hardness versus load characteristic of the as-cast alloys. It was found that the hardness first increases with increasing load and then it decreases or becomes constant after failure. This type of indentation behavior has been observed in almost all the as-cast alloys. The microhardness values of these alloys at various loads (i.e., 10, 25, 50, 100, 500, and 1000g) are given in Table 4.4. Also, I have measured indentation diagonal length by using ImageJ software. The Vickers hardness (in GPa) was calculated from the modified standard formula [167],

$$\mathbf{H = 1.654*9.81*P/d^2}$$

Where P is the load (g) and d is the indentation diagonal length in μm. A comparative study has been done for the comparison of hardness at an indentation load of 100g among all the as-cast alloys as shown in Fig. 4.17(a). The maximum and minimum Vickers hardness value was found to correspond to alloy-D and alloy-A and have values of ~13GPa and ~10GPa respectively while the mean hardness of the master alloy (grey cast-iron) is only ~2.8GPa. At the 100g indentation load the maximum and minimum reduced elastic modulus of the material was found to correspond to alloy-D and alloy-A and it has values of ~264 GPa and ~211 GPa respectively while the master alloy has only ~118 GPa. The elastic modulus and microhardness values with standard deviation of all as-cast alloys at 100g indentation load are given in Table 4.9.

Table 4. 7: Indentation diagonal length, microhardness data in GPa at various loads are displayed

	Indentation diagonal length, (µm)				**Vickers hardness (H_V) with std. dev. (in GPa)**				
Load(g)	**d_A**	**d_B**	**d_C**	**d_D**	**Alloy-A**	**Alloy-B**	**Alloy-C**	**Alloy-D**	**Remarks**
10	3	2.3	2.8	2.85	6.7±1	9±1	7.2±0.9	9±1.9	No cracks
25	5.5	4.65	5.8	5	8.5±0.8	9±1.4	8±1	10.7±2	No cracks
50	8.5	7.5	8.2	7.69	9±0.9	10.7±0.9	10.5±0.8	10.5±3	No cracks
100	12.5	11.35	13	11.45	10±0.5	11.5±0.8	10.8±0.8	12.6±1.3	No cracks
500	28.5	27	29.1	28.33	10.5±0.8	11.9±0.8	11±0.9	11.7±0.5	Palmqvist Crack in alloy-D
1000	43	39.15	41.05	39.5	10±0.7	12±0.2	11.5±0.5	11.9±0.6	Palmqvist Crack in alloy-B and D

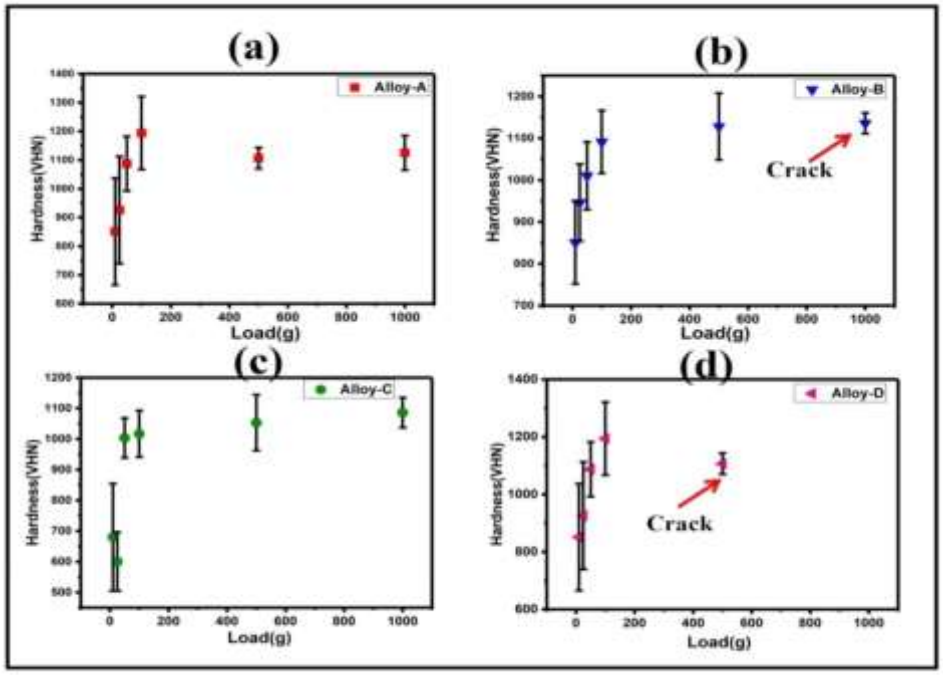

Fig. 4. 14: Variation of hardness (VHN) concerning load (g) for the Cu-mould cast alloys (a) alloy-A, (b) alloy-B, (c) alloy-C, and (d) alloy-D (arrows marks showing cracks occur at that load)

4.3.6 Determination of Indentation Fracture Toughness (K_{IC})

It was observed in alloy-B and alloy-D, that very fine radial cracks appeared from the indentation corner at 1000g indentation load as shown in Fig. 4.15 (a-b). For evaluating the fracture toughness of these materials the Palmqvist method[168], [169] was used. The fracture toughness of any brittle material can be estimated by using the expression written below.

$$K_{IC} = 0.035\Phi^{(-3/5)} H_v (a / L^{1/2}) (H/E)^{-2/5}$$

Where K_{IC} = Indentation fracture toughness, Φ=Constraint factor and has been taken 2.5[170], H_v=Vickers microhardness (GPa), E=Young's modulus (GPa), a = half of the indentation size (in μm), and L=length of Palmqvist crack. There are various factors were considered for the estimation of the fracture toughness using the Palmqvist crack method are reported elsewhere[170]–[172]. The fracture toughness of as-cast alloys is given in Table 4.8.

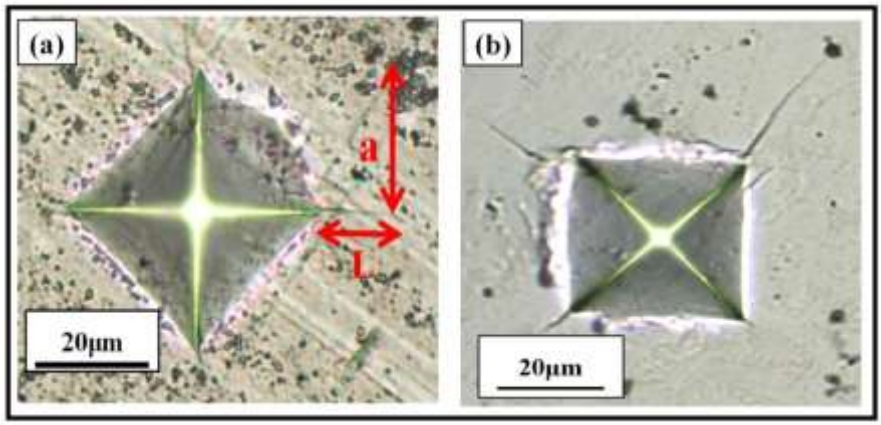

Fig. 4. 15: Optical micrographs showing indentation impression with a radial crack on (a) alloy-B and (b) alloy-D at a 1000g load

Table 4. 8: Fracture toughness of Cu-mould cast alloys at a load of 1000g

Sample	Estimation method	Crack length (a) (μm)	Fracture toughness (K_{IC}) MPa. $(m)^{1/2}$
Alloy-B	Palmqvist method	11.5	4.22
Alloy-D	Palmqvist method	25.7	3.73

4.3.7 Determination of Yield strength (σ_o), Meyer's exponent (n), material constant (K)

The hardness values allow us to calculate the 0.2% offset yield strength. This can be determined by employing the following expression[173];

$$\sigma_o = (VHN/3)0.1^{n-2}$$

Where σ_o = 0.2% offset yield strength and n is Meyer's exponent or related to the capacity of work hardening. The variation of hardness with load can be also analyzed using Meyer's law. The variation of load can be related to the diagonal length (d) as;

$$P = Kd^n$$

Where P is the applied load (in Kg), d is the indentation diagonal length (in mm), K is the material constant related to the resistance of the metal to penetration, and n is Meyer's exponent. In the ideal case, n attains a value of 2. However, the value of n varies from material to material. It is a worthwhile exercise to determine these parameters for our alloys and understand their behavior. Such attempts have been also made in the past for other system[174]–[176]. From our present experimental data, I have plotted LogP versus Log d curves for the as-cast alloys A, B, C, and D as shown in Fig. 4.16(a-d). The values of

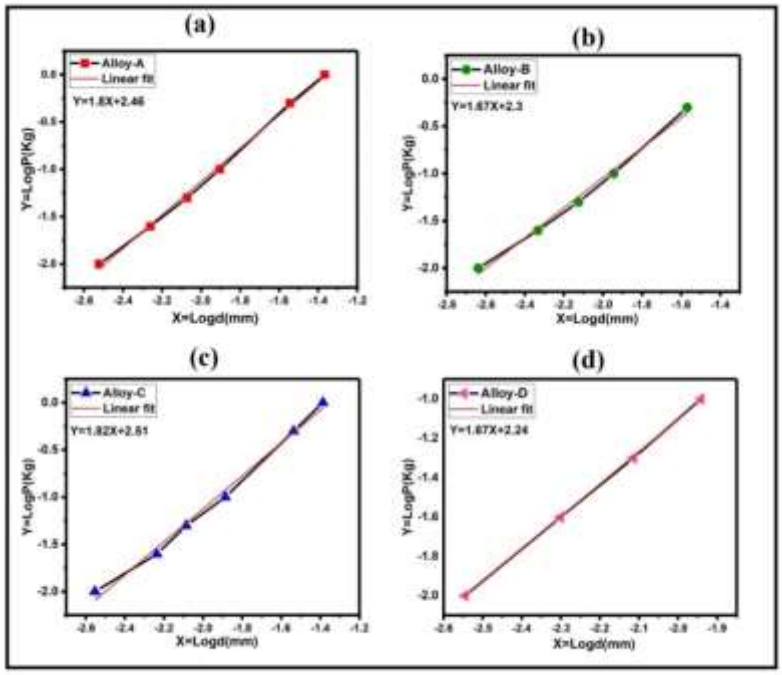

Fig. 4. 16: Log P vs Log d plots for Cu-mould cast alloys (a) alloy-A, (b) alloy-B, (c) alloy-C, and (d) alloy-D. The lines are the linear fit to the data and R^2 is the correlation coefficient having values of ~ 0.99

exponent and Log K are given in Table 4.9. It was observed that the value of exponent n is less than 2 for all as-cast alloys. The Meyer exponent values for all the alloys are different. This change is due to microstructural and structural variations in them. The Meyer exponent for alloy-C is highest (n=1.82) and the ratio of VHN/σ_o is also highest (=1.98). With the help of Meyer's exponent and equations as described above, I have estimated σ_o, and their values are given in Table 4.9. It may be observed that σ_o is the maximum for alloy-D (=9.26 GPa).

Table 4. 9: Values of average VHN, E, n, Log K, and σ_o of as-cast alloys at 100g load

As-cast alloys	VHN(H_v) (GPa) (100g load)	Reduced Elastic modulus (E)(GPa)	n	LogK	σ_o (GPa) (100g load)	VHN/σ_o
A	10	211	1.80	2.46	5.28	1.89
B	11.5	243	1.67	2.30	8.19	1.40
C	11	262	1.82	2.51	5.55	1.98
D	13	264	1.67	2.24	9.26	1.40

4.5.8 Determination of Plastic criterion (R_w), and Percentage of Elastic recovery (%R)

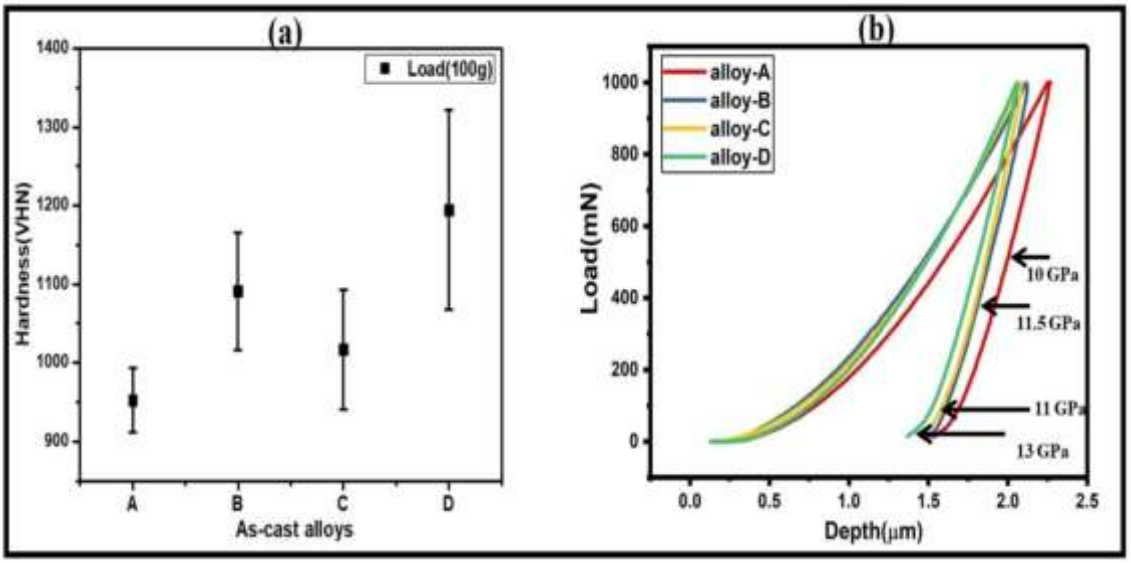

Fig. 4. 17: (a) Comparison of hardness (VHN) at indentation load of 100g among all alloys processed through Cu-mould casting and (b) Load-displacement (P-h plot) response of as-cast alloys at 100g indentation load

The load-displacement (P-h) curves for the alloys are shown in Fig. 4.17 (b). The depth of penetration for alloys A, B, C, and D are 2.26, 2.12, 2.08, and 2.06μm respectively. Higher the

slopes of unloading curve in the P-h plot represent higher stiffness of the alloys. The net amount of work done during an indentation test can be estimated by the area enclosed by the p-h curve.

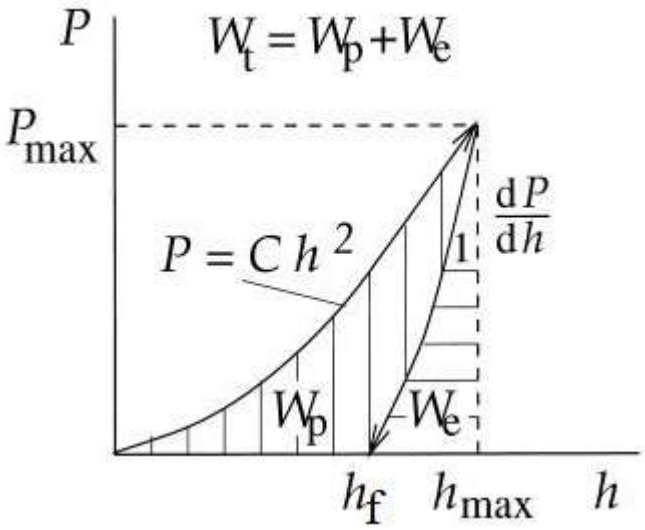

Fig. 4. 18: P-h curve for loading and unloading, and their associated nomenclature[177]

The indentation experiment also provides a suitable way to measure the magnitude of plastic deformation. A schematic representation of the P-h curve is shown in Fig. 4.18, which represents the nomenclature of associated parameters that are to be used for the calculation of deformation. Three important parameters were calculated from the P-h curves. A plastic criterion R_w[178], [179] is defined as the ratio of plastic work (W_p) to total work ($W_T = W_P + W_e$) and this ratio is expressed as a percentage and is given by

$$\% R_W = (W_P / W_T) 100$$

The elastic recovery (R)[120] can be defined as the ratio of the final depth of the indentation (h_f) to the maximum penetration depth (h_{max}) of the indenter,

$$\text{Elastic recovery } R = h_f/h_{max}$$

And percentage of elastic recovery (%R)[120] of displacement on the unloading curve can be expressed as:

$$\%R = [(h_{max} - h_f)/h_{max}) 100\%]$$

The parameter R_W was found that for all the alloys above 50%, it indicates that plastic deformation is more dominant as compared to elastic deformation. Alloy-C has a maximum value of R_W (~65%), and it has a good amount of plasticity among all. The limit of elastic recovery generally lies in the range of $0 \leq h_f/h_{max} \leq 1$, where the lower limit corresponds to fully elastic deformation and the upper limit reflects characteristics of rigid plastic materials for which there is no elastic recovery. The values of these parameters are given in Table 4.10.

The ratio of hardness to elastic modulus (H/E) is an important parameter that can measure the degree of elastic recovery. The H/E value is maximum for alloy-D (=0.049), which indicates that elastic recovery is more in the alloy-D. The value of hardness to density ratio (H/ρ), and specific stiffness (E/ρ) is also higher for the alloy-D. I have estimated these parameters for all the as-cast alloys and their values are given in Table 4.11.

Table 4. 10: The Mechanical properties of the tested alloys estimated from the P-h plot at 100g indentation load

Alloys	W_P (10^{15} J)	W_e (10^{15} J)	W_T (10^{15} J)	R_W (in %)	h_f (µm)	h_{max} (µm)	h_f/h_{max}	%R
A	446.26	297.14	743.41	60	1.54	2.25	0.68	31.5
B	415.93	250.05	665.98	62.5	1.50	2.12	0.77	29.2
C	436.23	233.61	669.85	65	1.45	2.08	0.69	30.3
D	386.86	247.42	634.28	61	1.37	2.05	0.66	33.2

Table 4. 11: Some important Mechanical properties of Cu-mould cast alloys at 100g load

Alloys	H (GPa)	E (GPa)	H/E	H/ρ	E/ρ
A	10	211	0.047	1.34	28.2
B	11.5	243	0.047	1.50	31.7
C	11	262	0.042	1.47	35
D	13	264	0.049	1.78	36

4.4 Discussions

4.4.1 Microstructure, Phase/Structure Analysis

Based on XRD results, it was confirmed that the above alloys produced through arc-melting followed by simple Cu-mould casting are not amorphous. Although these are good glass in literature[120]–[122], [148], [180]. The reason behind the failure to get amorphous steel may have two aspects, they refer to (i) the selection of raw material, and (ii) the selection of the processing route (simple Cu-mould casting). I have taken grey cast iron (~50%) as a raw material and added elements in pure (~99%) form to make alloys. In literature, they are using these elements either in pure form or in pre-alloyed form[120], [121], [180], [181]. It was observed by many researchers, that the usage of industrial raw materials tends to decrease the glass-forming ability due to the negative role of contained impurities[32], [71]. For the making of BMGs, people are using various processing techniques like suction casting, drop casting, injection casting, suction casting-into-Cu-mould casting, etc.[4]. Alloy-A has produced a non-uniform microstructure, some region shows a dendritic structure and somewhere pearlite is formed in the cementite matrix. It may be due to variations in the cooling rate inside the Cu-mould. However, after alloying addition in alloy-B, alloy-C, and alloy-D spheroidized carbides are formed in the ferrite matrix. The size of these carbide particles in alloy-B, alloy-C, and alloy-D are in the range of 6-11μm, 3-7μm, and 2-4μm respectively. Variation in microstructure has been seen due to alloying addition and cooling rate. Iqbal et al., [120] also found dendritic microstructure after annealing of Fe-Cr-Mo-C-B-Y BMGs.

The XRD result of alloys processed through Cu-mould casting shows multiple crystalline peaks with various phases $Fe_{11}Mo_6C_5$ (mC44), α-Fe (cI2), Fe_5C_2 (mC28), Fe_3C (oP116), Fe_3W_3C (cF112), and Cr_7C_3 (oP40). Some of these phases are common in them. Some new phases were evolved in alloy-A, alloy-B, and alloy-C whose d-spacing is matched with carbides of Fe_5C_2 (mC28), Fe_3W_3C (cF112), and Fe_3C (oP16) type of structures respectively. Most of these phases are also observed by many researchers[40], [122], [182]–[184] after the annealing process. All the information regarding phases that are evolved in the samples processed through the Cu-mould casting technique is given in Table 4.12.

The melting temperatures of these alloys were found from DTA thermograms. The melting temperatures of alloys A, B, C, and D are 1035°C, 1135°C, 1130°C, and 1145°C respectively. These alloys have nearly similar melting point values which are also governed by the above composition of alloys in the BMGs form[40], [121], [122], [148].

Table 4. 12: Detail information of the phases evolved in the alloys processed through Cu-mould casting

Sl.no.	Phase obtained	Pearson symbol	Space group (no.)	Samples	JCPDS no.
1	$Fe_{11}Mo_6C_5$	mC44	C2/m (12)	All	01-089-2311
2	Cr_7C_3	oP40	Pnma (62)	All	01-089-7244
3	Fe_5C_2	mC28	C2/c (15)	Alloy-A,	00-051-0997
4	Fe_3C	oP116	Pnma (62)	Alloy-C	01-077-0255
5	Fe_3W_3C	cF112	Fd-3m (227)	Alloy-B	00-041-1351
6	α-Fe	cI2	Im-3m (229)	All	00-006-0696

4.4.2 Indentation Characteristics Analysis

The Vickers micro-indentation experiment was carried out for the investigation of the nature of indentation for the Cu-mould cast alloys. The indentation impression of alloy-A and alloy-C have been found regular and crack-free up to the applied load of 1000g, while alloy-B holds up to 500g only and a fine crack has appeared at the corner of the indentation mark at the load of 1000g. Alloy-D also has a fine crack at the load of 500g. The nature of these cracks is Palmqvist type. Alloy-B exhibits maximum indentation fracture toughness (= 4.22 MPa.$m^{1/2}$) at 1000g applied load. The increase in the fracture toughness of alloy-B can be attributed to the inhibition of cracks due to the formation of a new phase Fe_3W_3C that was missing in alloy-D. The crack length was found to almost double in alloy-D. The average fracture toughness value for these alloys was found to be greater than the composition of BMGs $Fe_{41}Co_7Cr_{15}Mo_{14}C_{15}B_6Y_2$ (3.73 MPa.$m^{1/2}$) reported by Keryvin et al.[185], Fe-Mn-P-B-C (1.91 MPa.$m^{1/2}$)[186] and BMG composite Fe-Co-Nb-B (2.9 MPa.$m^{1/2}$)[172]. The absence of cracks around the indented area of alloy-A and alloy-C indicates better toughness of these alloys as compared to others. Alloy-A has a maximum depth of penetration (~2.25μm) among all the as-cast alloys at 100g indentation load. The P-h curve states that the indentation depth increases with decreasing the hardness. The indentation size increases regularly with the indentation load. It was found that hardness first increases with increasing load and then it decreases or becomes constant after reaching a critical value. The

maximum Vickers microhardness was observed in alloy-D (~1327) and reduced elastic modulus (~275 GPa). However, the minimum hardness was observed in alloy-A (~995) and minimum elastic modulus (~189 GPa) at 100g indentation load. The indentation characteristics results can be compared with Lu's steel[40], they find the hardness and elastic modulus values 1224 and 257 GPa respectively. Microhardness, Young's moduli of the present steels were found to be higher than many BMGs[123], [158], [163], [187]. The 0.2% offset of yield strength (σ_o) was also found maximum for alloy-D (=9.26 GPa). The high hardness and yield strength value observed in alloy-D may be due to the finer microstructure observed in alloy-D. Therefore, it is expected that the microstructural variation may be one of the factors that is responsible for the increase in the hardness value in this alloy. There are many such findings available in the literature to support this aforesaid statement[188]–[190]. I have to find Meyer's index (n)[175][191], for as-cast alloys from Log(P) vs Log(d) plot, the value of n is evaluated in the range of 1.67-1.82 (i.e. $n < 2$).

The indentation experiment also provides a sustainable way to measure the magnitude of deformation. The area under the P-h curve, which provides a measure of elastic and plastic energy components of deformation during indentation[177].Three important parameters plastic criterion (R_w), elastic-recovery (R), and percentage of elastic recovery (%R) were calculated from P-h plots. The value of elastic recovery ($R=h_f/h_{max}$) for Cu-mould cast alloys is in the range of 0.66-0.77, while the percentage of elastic recovery (%R) ranges from 29.2%-33.2%. The maximum elastic recovery was found to correspond to alloy-C (~0.77) and the percentage of elastic recovery corresponded to alloy-D (~33.2%). The maximum indentation work done for elastic work recovered during the indentation test is observed for alloy-A (~40%) and the plastic response of this alloy is ~60%. The H/E ratio is an important parameter that is used to measure the degree of elastic recovery[167]. The H/E value is obtained maximum for alloy-D (=0.049), which indicates that elastic recovery is greater in this alloy. The hardness-to-density ratio (H/ρ) of present alloys was found to be 1.34, 1.44, 1.47, and 1.78 in alloy-A, alloy-B, alloy-C and alloy-D respectively. The H/ρ ratio in amorphous steel[40] and maraging steel[192] are found to be 1.64 and 0.52 respectively. The H/ρ ratio of present steel was found to be ~4 times higher than maraging steel and it is comparable to amorphous steel. The maximum specific stiffness (E/ρ) among the alloys is found in alloy-D (~36). The specific stiffness is also much higher than maraging steel (~18.64) and comparable to amorphous steel (~32). This aspect may be useful for designing engineering components for specific applications.

4.5 Conclusions

Based on the results described and discussed in this Chapter, the following conclusions can be drawn:

(i) Four different alloy steels $Fe_{56.24}Cr_4Mo_{14}C_{15}Si_{3.8}B_6$ (A), $Fe_{43.47}Cr_{15}Mo_{14}C_{15.12}Si_{3.78}B_6Y_2$ (B), $Fe_{40.2}Cr_{20}Mo_{10}W_2C_{15}Si_{4.2}B_6Y_2$(C) and $Fe_{40.2}Cr_{15}Mo_{14}Co_3C_{15}Si4_{.2}B_6Y_2$ (D) were produced by arc-melting followed by Cu-mould casting technique. These alloys are crystalline. Alloy-A having a nominal composition of $Fe_{56.24}Cr_4Mo_{14}C_{15}Si_{3.8}B_6$ has produced a non-uniform microstructure of dendritic and Pearlite, while a uniform microstructure of spheroidized carbides is formed in ferrite matrix in other alloys.

(ii) The phases evolved in these alloys are, α-Fe (cI2), $Fe_{11}Mo_6C_5$ (mC44), Cr_7C_3 (oP40), Fe_5C_2 (mC28), Fe_3C (oP116), and Fe_3W_3C (cF112). Some of these phases are also observed in various amorphous steels in literature after the annealing process.

(iii) The Palmqvist type of cracks are observed in alloy-B and alloy-D at 1000g and 500g of applied load respectively. The absence of cracks in alloy-A and alloy-C shows high ductility in them. The average fracture toughness in alloy-B and alloy-D are found 4.22 MPa.$m^{1/2}$ and 3.73 MPa.$m^{1/2}$.

(iv) The high hardness and Yield strength value was observed in alloy-D ~1327(VHN), and 9.26 GPa respectively. It was also observed that reduced elastic modulus (~275 GPa) is higher in alloy-D. It may be due to the finer microstructure observed in alloy-D. The maximum depth of penetration was found in alloy-A (~2.25 μm), therefore minimum hardness was found (~995 GPa) to correspond to this.

(v) The value of elastic recovery ($R=h_f/h_{max}$) for these alloys are in the range of 0.66-0.77, while the percentage of elastic recovery (%R) ranges in 29.2%-33.2%. The H/E value is obtained maximum for alloy-D (=0.049), it indicates that elastic recovery is more in this alloy-D.

(vi) The hardness-to-density ratio (H/ρ) and specific stiffness (E/ρ) are found maximum for alloy-D, 1.78 and 36 respectively. The H/ρ ratio of the present alloy was found to be ~4 times higher than maraging steel[192] and it is comparable to amorphous steel[40]. The E/ρ is also much higher than maraging steel (~18.64) and comparable to amorphous steel (~32).